Research paper

Insights into the size effect of ZnCr$_2$O$_4$ spinel oxide in composite catalysts for conversion of syngas to aromatics

Yi Fu [a,b], Youming Ni [a], Wenhao Cui [a,b], Xudong Fang [a,b], Zhiyang Chen [a], Zhaopeng Liu [a,b], Wenliang Zhu [a,*], Zhongmin Liu [a,b,*]

[a] National Engineering Laboratory for Methanol to Olefins, Dalian National Laboratory for Clean Energy, Dalian Institute of Chemical Physics, Chinese Academy of Sciences, Dalian, 116023, Liaoning, China
[b] University of Chinese Academy of Sciences, Beijing, 100049, China

Abstract

Direct conversion of syngas to aromatics (STA) over oxide-zeolite composite catalysts is promising as an alternative method for aromatics production. However, the structural effect of the oxide component in composite catalysts is still ambiguous. Herein, we investigate the size effect by selecting ZnCr$_2$O$_4$ spinel, as a probe oxide, mixing with H-ZSM-5 zeolite as a composite catalyst for STA reaction. The CO conversion, aromatics selectivity and space-time yield (STY) of aromatics are all significantly improved with the crystal size of ZnCr$_2$O$_4$ oxide decreases, which can mainly attribute to the higher oxygen vacancy concentration and thus the rapid generation of more C$_1$ oxygenated intermediate species. Based on the understanding of the size−performance relationship, ZnCr$_2$O$_4$-400 with a smaller size mixing with H-ZSM-5 can achieve 32.6% CO conversion with 76% aromatics selectivity. The STY of aromatics reaches as high as 4.79 mmol g_{cat}^{-1} h^{-1}, which outperforms the previously reported some typical catalysts. This study elucidates the importance of regulating the size of oxide to design more efficient oxide-zeolite composite catalysts for conversion of syngas to value-added chemicals.

1. Introduction

Developing new routes for the effective utilization of non-petroleum carbon resources (such as coal, biomass, natural gas, and waste) to produce clean fuels and value-added chemicals is of great interest due to the shortage of petroleum resources and the environmental problems [1]. Aromatics, acting as significant bulk chemicals, are widely applied for the production of solvents, medicines, dyes and polymers in the chemical industry [2]. Currently, aromatics are mainly obtained by the petroleum refining process, which is environmentally unfriendly and energy-intensive [3,4]. Catalytic conversion of syngas (a mixture of CO/H$_2$) derived from aforementioned non-petroleum resources into aromatics has attracted extensive attention because of its prominent function in sustainable development [5]. By means of the well-known Fischer−Tropsch synthesis (FTS), various hydrocarbons can be produced from syngas, but almost no aromatics can be obtained due to the limitation of Anderson-Schulz-Flory distribution (ASF) [6,7]. The composite catalysts which integrating Fe-based FTS catalyst with H-ZSM-5 zeolite (such as Fe−Pd/H-ZSM-5 [8], Fe−MnO/GaZSM-5 [9], Na−Zn−Fe$_5$C$_2$/H-ZSM-5 [10], and Fe$_3$O$_4$@MnO$_2$/H-ZSM-5 [11]) is a useful means to optimize the aromatization performance. However, their aromatics selectivity is still unsatisfactory.

* Corresponding authors.
  E-mail addresses: wlzhu@dicp.ac.cn (W. Zhu), liuzm@dicp.ac.cn (Z. Liu).

Recently, an effective oxide-zeolite (OX−ZEO) bifunctional composite catalysts design strategy has been put forward to directly synthesize aromatics from syngas (STA reaction), among which CO and H_2 are activated into C_1 oxygenated intermediates over metal oxides, while the zeolite is mainly responsible for C−C coupling [12–19]. For example, Wang et al. [12]. Reported a composite catalyst combining Zn−ZrO$_2$ oxide with H-ZSM-5 zeolite could obtain 80% aromatics selectivity at 20% CO conversion. Bao et al. [13]. Presented that a composite catalyst integrating $ZnCrO_x$ oxide with H-ZSM-5 zeolite could achieve about 73.9% aromatics selectivity at 16% CO conversion. Nevertheless, the catalytic performance still needs to be further improved to meet the demands of industrial production, which will depend on the in-depth comprehending of the structure−performance relationship.

Previous studies have pointed out that the structure (such as crystal size) of the H-ZSM-5 zeolite in composite catalysts has a great influence on the catalytic performance for STA reaction [19,20]. Wei et al. [19] reported that the H-ZSM-5 with short size along the b-axis presented low molecular-diffusion resistance, leading to high selectivity of tetramethylbenzene. Xie et al. [20] observed that the light aromatics selectivity is closely related to the crystal size of H-ZSM-5, which could be enhanced by increasing the size of the b-axis. In comparison, there is little knowledge about the influence of the oxide structure in composite catalysts for STA reaction. Generally, the oxide with a smaller size can result in more defect sites (oxygen vacancies) [17,21], and it has been reported that oxygen vacancies over metal oxide surfaces are conducive to CO hydrogenation activation [1,16,22]. Therefore, we wondered whether oxide with a smaller size will have a beneficial effect on the catalytic performance. However, little in-depth research about the size effect of oxide component in composite catalysts for STA reaction has been reported.

In this work, we investigate the size effect by selecting $ZnCr_2O_4$ spinel oxide, which is often used for syngas conversion, as a probe oxide, mixing with H-ZSM-5 zeolite as a composite catalyst for STA reaction. To achieve this goal, a series of $ZnCr_2O_4$ spinel oxides with distinct size were synthesized, and we compared the catalytic performance of this series of $ZnCr_2O_4$&H-ZSM-5 composite catalysts as a function of size of $ZnCr_2O_4$. We further reveal the intrinsic reason of the size effect by *in situ* DRIFTS characterizations. Moreover, by decreasing the crystal size of $ZnCr_2O_4$ oxide, the space-time yield (STY) of aromatics can reach as high as 4.79 mmol g_{cat}^{-1} h^{-1}, which outperforms the previously reported some typical composite catalysts (Fig. S1 and Table S1).

2. Experimental section

2.1. Catalyst preparation

A series of $ZnCr_2O_4$ spinel oxides with diverse sizes were synthesized by employing a conventional co-precipitation method. Typically, 48 g of $Cr(NO_3)_3 \cdot 9H_2O$ and 17.85 g of $Zn(NO_3)_2 \cdot 6H_2O$ were dissolved in 100 mL of deionized water

to make a salt solution, and 47.10 g of ammonium carbonate $(NH_4)_2CO_3$ was added in 100 mL of deionized water to prepare a precipitant solution. After that, two peristaltic pumps were used to simultaneously inject the above two solutions into a beaker at 70 °C under persistent stirring to form a precipitate. Meanwhile, the pH value of the blended solution was maintained at around 7.0 by adjusting the flow rate of the two peristaltic pumps. After precipitation, the synthesized mixture was further aged for 5 h at the same temperature. Then the suspension was filtered and washed with deionized water several times to obtain a filter cake, which followed by drying overnight at 120 °C and finally calcined in air with a heating rate of 2 °C·min^{-1} for 6 h. The resulting powder oxides with different sizes were denoted as $ZnCr_2O_4$-T, where T representing the calcination temperature, which varied from 400 to 700 °C. For example, $ZnCr_2O_4$-400, $ZnCr_2O_4$-500, $ZnCr_2O_4$-600 and $ZnCr_2O_4$-700 represent samples calcined at 400, 500, 600 and 700 °C, respectively.

H-ZSM-5 zeolite with a Si/Al ratio of 96 used in this work was the same as our previous study [17,23]. The detailed physical properties of this H-ZSM-5 zeolite are exhibited in Fig. S2 and Table S2, which embraces a typical nano-sized MFI structure. All the composite catalysts were acquired by physical mixing of the two components (oxides and zeolites) with a mass ratio of 3:1. For example, for the preparation of the $ZnCr_2O_4$-400&H-ZSM-5 composite catalyst, $ZnCr_2O_4$-400 oxide and H-ZSM-5 zeolite were firstly placed in an agate mortar and triturated together into powder, then followed by pressing under 30 MPa, crushed, and finally screened to granules between 40 and 60 mesh sizes (0.3−0.45 mm).

2.2. Characterization of catalysts

The powder X-ray diffraction (XRD) data were obtained on a PANalytical X'Pert PRO X-ray diffractometer equipped with a Cu Kα radiation source radiation (λ = 1.5406 Å). XRD patterns were measured in the 2 theta range of 5-90°. The average crystal size of $ZnCr_2O_4$ spinel oxides was calculated according to the Scherrer equation by selecting the two representative diffraction peaks at 30.3° and 35.8°, which correspond to the (022) and (113) lattice planes of spinel cubic $ZnCr_2O_4$, respectively.

The chemical composition was determined on a Philips Magix-601 X-ray fluorescence (XRF) spectrometer. The micropore volume, BET specific surface areas and average pore width were recorded by N_2 adsorption−desorption at −196 °C using a Micromeritics ASAP 2020 system, the samples were pre-degassed in vacuum at 120 °C for 24 h before measurement. The morphology of catalysts was observed by utilizing a Hitachi SU8020 field-emission scanning electron microscope (FE-SEM). A JEM-2100F microscope was used to acquire the transmission electron microscopy images (TEM) and high-resolution transmission electron microscopy images (HRTEM). The average particle size of each sample was estimated by counting at least 50 particles. The X-ray photoelectron spectroscopy (XPS) was conducted on a Thermofisher Excalab X+ spectrometer with

monochromatized Al Kα as the exciting radiation, the binding energy of all the data was calibrated by utilizing the C 1s of 284.8 eV as the reference. The CO-temperature programmed desorption profiles (CO-TPD) were carried out by using a Micromeritics AutoChem II 2920 analyzer equipped with a TCD, helium and 10% CO−He were used for reference and adsorption, respectively. The H_2-temperature programmed reduction profiles (H_2-TPR) were performed on a Micromeritics AutoChem II 2920 analyzer equipped with a TCD, argon and 10% H_2−Ar were used for reference and reduction, respectively. The NH_3-temperature programmed desorption profiles (NH_3-TPD) were tested by a Micromeritics AutoChem II 2920 equipped with a TCD detector.

The *in situ* diffuse reflectance infrared Fourier transform spectroscopy (DRIFTS) measurements were performed on a Bruker Tensor 27 instrument equipped with a MCT detector to detect the change of intensity of surface intermediate species. Typically, a diffuse reflectance infrared cell with a ZnSe window was loaded with 50 mg of the sample, which was pretreated with 30 mL min^{-1} of H_2/N_2 flow (H_2/N_2 = 1/5) under 0.1 MPa at 310 °C and followed by sweeping with pure N_2 at a flow rate of 30 mL min^{-1}. After that, the temperature was heated up to 390 °C and the background spectrum was recorded. Then 5 mL min^{-1} of syngas (H_2/CO/Ar = 47.5/47.5/5) was introduced into the infrared cell under 0.1 MPa at 390 °C and the *in situ* DRIFT spectra were acquired at 16 scans with a resolution of 4 cm^{-1}.

2.3. Catalytic reaction

All the catalytic reactions were carried out in a high-pressure fixed-bed stainless steel tubular reactor (internal diameter of 8 mm). The reaction effluent products were heated to maintain in the gas phase and analyzed by an Agilent 7890B online gas chromatograph, which equipped with a thermal conductivity detector (TCD) connected to a TDX-1 packed column and a flame ionization detector (FID) connected to a PoraPLOT Q-HT capillary column. A concentration of 5% Argon contained in syngas was utilized as an internal standard gas. CO conversion and CO_2 selectivity were calculated according to the following equation based on the carbon atoms number.

$$\text{Sel}_{CO_2} = \frac{CO_{2outlet}}{CO_{inlet} - CO_{outlet}} \times 100\% \quad (1)$$

CO_2 outlet: moles of CO_2 at the outlet

$$\text{Conv}_{CO} = \frac{(CO_{inlet} - CO_{outlet})}{CO_{inlet}} \times 100\% \quad (2)$$

CO inlet: moles of CO at the inlet CO outlet: moles of CO at the outlet.

The selectivity of hydrocarbons (C_nH_m), MeOH and DME among the carbon products (excluding CO_2) were calculated according to the total carbon atoms of the products detected by FID detector.

$$\text{Sel}_{C_nH_m} = \frac{n_{C_nH_m}}{total\ carbon\ atoms\ of\ products\ detected\ by\ FID} \times 100\%$$

$$\text{Sel}_{MeOH} = \frac{n_{MeOH}}{total\ carbon\ atoms\ of\ products\ detected\ by\ FID} \times 100\%$$

$$\text{Sel}_{DME} = \frac{n_{DME}}{total\ carbon\ atoms\ of\ products\ detected\ by\ FID} \times 100\%$$

$$(3)$$

n_{CnHm}: carbon atoms number of C_nH_m
n_{MeOH}: carbon atoms number of MeOH
n_{DME}: carbon atoms number of DME

3. Results and discussion

3.1. Structural properties of the catalysts

A series of $ZnCr_2O_4$ oxides were prepared by a co-precipitation method at different calcination temperature [24], which were named as $ZnCr_2O_4$-T, where T representing the calcination temperature (see Experimental section). The XRD patterns (Fig. 1a) show that all $ZnCr_2O_4$ oxides are of the typical cubic $ZnCr_2O_4$ spinel phase (PDF #98-009-5832), but as the calcination temperature decreases from 700 °C to 400 °C (from $ZnCr_2O_4$-700 to $ZnCr_2O_4$-400), the full width half maximum (FWHM) broadens from the XRD analysis (Fig. 1a), suggesting that lowering the calcination temperature may lead to a decrease in the crystal size of $ZnCr_2O_4$ spinel oxides [25]. The calculation results from Scherrer equation further verify this speculation, the average crystal size of $ZnCr_2O_4$ spinel oxides changes dramatically from 32.1 to 7.9 nm (Table 1). The variation of the crystal size can attribute to the different crystallite growth rate in different calcination temperature [26,27].

The N_2 physical adsorption−desorption experiments (Fig. 1b) present that reducing the crystal size of $ZnCr_2O_4$ spinel oxides (from $ZnCr_2O_4$-700 to $ZnCr_2O_4$-400) can result in the formation of hysteresis loops, indicating the existence of mesopores, which may be caused by the stacking of oxides particles (Fig. S3). In addition, it can be seen from Table 1 that $ZnCr_2O_4$-700 with a larger size exhibits a very low BET specific surface area (8.63 m^2/g) and pore volumes (0.02 cm^3/g). Surprisingly, reducing the crystal size of $ZnCr_2O_4$ spinel oxides (from $ZnCr_2O_4$-600 to $ZnCr_2O_4$-400) can greatly increase the BET specific surface areas (~1.6−15 times) and pore volumes (~1.6−20 times).

The FE-SEM images (Fig. S3) and TEM images (Fig. 1c−f and Fig. S4) further provide convincing evidence that this series of $ZnCr_2O_4$ spinel oxides are consist of irregular nanoparticles with different particle sizes. The corresponding average particle sizes of $ZnCr_2O_4$ spinel oxides estimated by the TEM are 33.03 nm ($ZnCr_2O_4$-700), 16.63 nm ($ZnCr_2O_4$-600), 11.87 nm ($ZnCr_2O_4$-500) and 7.29 nm ($ZnCr_2O_4$-400), which is almost completely consistent with the average crystal size calculated by the Scherrer equation (Table 1). In addition,
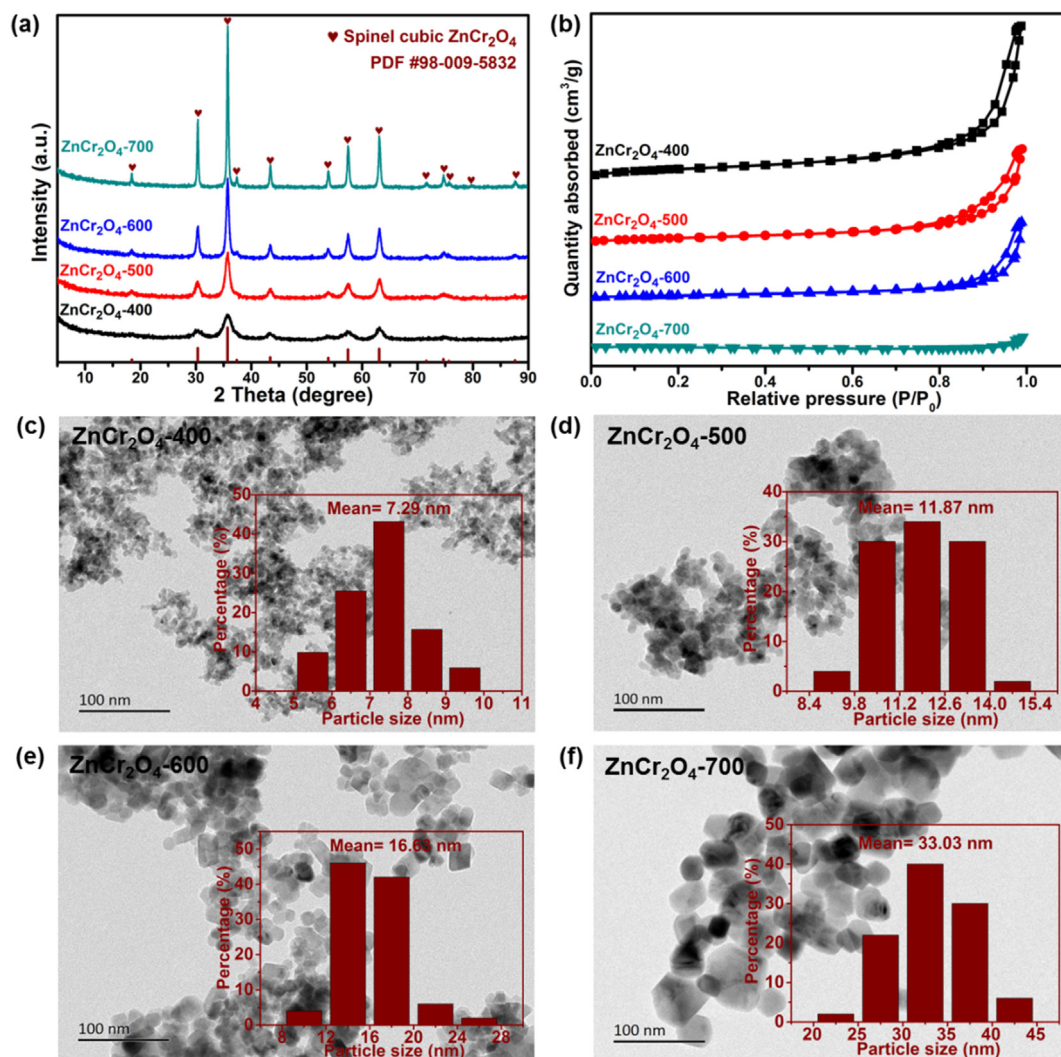
Fig. 1. Structural characterization of oxides. (a) XRD patterns of oxides. (b) N_2 adsorption−desorption isotherms of oxides (c−f) The TEM images and particle-size distribution (inset) of oxides. (c) $ZnCr_2O_4$-400 oxide, (d) $ZnCr_2O_4$-500 oxide, (e) $ZnCr_2O_4$-600 oxide, (f) $ZnCr_2O_4$-700 oxide, respectively. The scale bar represents 100 nm.

the lattice spacing of 0.208, 0.251, 0.295, and 0.480 nm in HRTEM images (Fig. S5) can be ascribed to the (004) (113) (022), and (111) planes of $ZnCr_2O_4$ spinel phase (PDF #98-009-5832), respectively. This further indicates that this series of $ZnCr_2O_4$ oxides are of the typical cubic $ZnCr_2O_4$ spinel structure.

Generally, the oxide with a smaller size and larger specific surface area can result in more surface defect sites (oxygen vacancies) [17,21], which are widely considered as active sites for CO hydrogenation activation [1,16,22,28,29]. To explore the concentration of oxygen vacancy over oxides, we performed X-ray photoelectron spectroscopy (XPS)

Table 1
The structural properties of oxides.

Oxides	BET surface area [a] (m^2/g)	Pore volume [a] (cm^3/g)	Average pore width [a] (nm)	Average crystal size [b] (nm)	Average particle size [c] (nm)	Oxygen vacancy concentration [d] (%)
$ZnCr_2O_4$-400	129.20	0.40	12.29	7.9	7.29	49.09
$ZnCr_2O_4$-500	78.83	0.25	12.51	11.3	11.87	41.69
$ZnCr_2O_4$-600	47.32	0.16	13.26	16.9	16.63	33.36
$ZnCr_2O_4$-700	8.63	0.02	7.02	32.1	33.03	26.17

[a] by N_2 physical adsorption−desorption.
[b] The average crystal sizes are calculated by the Scherrer equation.
[c] The average particle sizes are estimated by the TEM.
[d] The oxygen vacancy concentration of oxides calculated from the deconvolution of O 1s XPS signal (for a detailed description, see Table S3 in the Supporting Information).

measurements. As clearly depicted in Fig. 2a, two diverse signal peaks can be recognized from the O 1s XPS spectra of $ZnCr_2O_4$ oxides. One peak at a lower binding energy of 530.0 ± 0.3 eV can be regarded as the lattice oxygen atoms ($O_{lattice}$) [30], while another peak situated at a higher binding energy of 531.0 ± 0.3 eV can usually be attributed to the oxygen atoms in the vicinity of the oxygen vacancy ($O_{vacancy}$) [29,31]. Obviously, the ratios of the $O_{vacancy}$ peak for these oxides are distinct, indicating that their corresponding oxygen vacancy concentration could be quite disparate. On the basis of the calculated results from the deconvolution of the O1s XPS signal (Table 1 and Table S3) [32], the $ZnCr_2O_4$-400 exhibited the highest oxygen vacancy concentration, followed by $ZnCr_2O_4$-500, $ZnCr_2O_4$-600, and $ZnCr_2O_4$-700. It is not surprising that $ZnCr_2O_4$-400 owns more surface vacancies than the other three oxides due to its smaller size and larger specific surface area.

Furthermore, we performed CO temperature-programmed desorption (CO-TPD) experiments to investigate the adsorption and desorption behaviors of CO on the $ZnCr_2O_4$ oxides. As shown in Fig. 2b, the low-temperature peak (<300 °C) can be attributed to the weak adsorption of CO in the bulk phase, whereas the high-temperature peak (> 300 °C) can be linked to the CO strongly absorbed at the oxygen vacancies [33−35]. The amount of CO desorption follows this order: $ZnCr_2O_4$-400 > $ZnCr_2O_4$-500 > $ZnCr_2O_4$-600 > $ZnCr_2O_4$-700, indicating that the oxygen vacancy concentration also follows the same order, which is quite consistent with the XPS results (Fig. 2a and Table 1). Moreover, it has been widely reported that stoichiometric $ZnCr_2O_4$ spinel (normal spinel) is hard to reduce [19,36]. However, the existence and increase of the oxygen vacancies could promote the reducibility of $ZnCr_2O_4$ spinel oxides [19,36]. Therefore, the sharp reduction peak in the temperature range of 200−350 °C (Fig. 2c) could be assigned to the $ZnCr_2O_4$ spinel oxides with oxygen vacancies [19,36]. Distinctly, the reduction peak intensity also follows this order: $ZnCr_2O_4$-400 > $ZnCr_2O_4$-500 > $ZnCr_2O_4$-600 > $ZnCr_2O_4$-700, which further demonstrates the difference of oxygen vacancy concentration (Table 1).

3.2. Catalytic results and size−performance relationship

The above characterization results demonstrate that we have successfully prepared a series of $ZnCr_2O_4$ spinel oxides with different size and surface defect sites. Then, we wondered whether these oxides with their unique structural properties would affect the activity and product selectivity for STA reaction. Therefore, $ZnCr_2O_4$ spinel oxides with distinct size were blended with the same H-ZSM-5 as composite catalysts for STA reaction at 390 °C, 3.0 MPa, oxides: H-ZSM-5 = 3:1
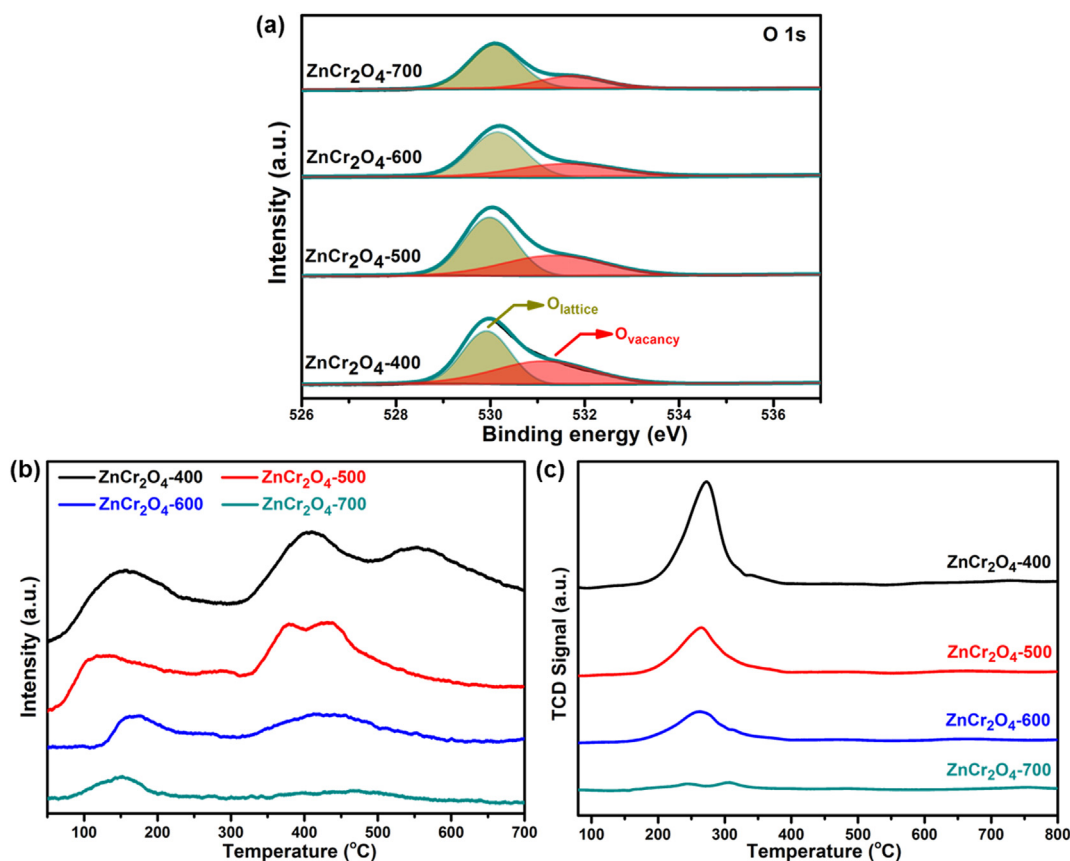

Fig. 2. Structural characterization of oxides. (a) The O 1s XPS spectra of oxides. $O_{lattice}$ is denoted as the lattice oxygen atoms, $O_{vacancy}$ is denoted as the oxygen atoms in the vicinity of the oxygen vacancy. (b) CO-temperature programmed desorption profiles (CO-TPD) of oxides. (c) H_2-temperature programmed reduction profiles (H_2-TPR) of oxides.

Table 2
Catalytic results for syngas conversion over a series of ZnCr$_2$O$_4$&H-ZSM-5 composite catalysts.

catalyst	CO Conv. (%)	CO$_2$ Sel. (%)	Selectivity of products (%)						STY of aromatics (mmol g$_{cat}^{-1}$ h^{-1})
			CH$_4$	C$_{2-4}^0$	C$_{2-4}^=$	C$_5^+$	Aromatics	MeOH& DME	
ZnCr$_2$O$_4$-400&H-ZSM-5	32.6	46.9	2.1	12.2	2.9	6.8	76.0	0.1	4.40
ZnCr$_2$O$_4$-500&H-ZSM-5	23.0	47.8	1.8	12.4	4.1	8.3	73.3	0.1	2.94
ZnCr$_2$O$_4$-600&H-ZSM-5	14.7	48.0	2.9	11.5	5.7	9.5	70.2	0.2	1.80
ZnCr$_2$O$_4$-700&H-ZSM-5	3.4	46.5	11.0	21.9	9.1	7.6	50.4	0	0.31

Reaction conditions: T = 390 °C, 3.0 MPa, H$_2$/CO/Ar = 47.5/47.5/5, Space velocity = 1500 mL g$_{cat}^{-1}$ h^{-1}, Oxides: H-ZSM-5 = 3:1. Note that C$_{2-4}^=$ and C$_{2-4}^0$ refer to C$_{2-4}$ olefins and paraffins, respectively. The C$_5^+$ excludes aromatics. The STY (space-time yield) of aromatics represents mmoles of aromatics generated per gram of catalyst per hour.

(mass ratio) and GHSV = 1500 mL g$_{cat}^{-1}$ h^{-1}. The results in Table 2 and Fig. S6 indicate that this series of ZnCr$_2$O$_4$&H-ZSM-5 composite catalysts exhibit obviously different catalytic performance. From ZnCr$_2$O$_4$-700&H-ZSM-5 to ZnCr$_2$O$_4$-400&H-ZSM-5, the CO conversion, aromatics selectivity and STY of aromatics are significantly promoted. Since the zeolite components for all the composite catalysts are completely consistent, it can be reasonably inferred that the difference in reaction results is mainly related to the difference in the structural properties of the ZnCr$_2$O$_4$ spinel oxides.

Therefore, we compared the catalytic performance of this series of ZnCr$_2$O$_4$&H-ZSM-5 composite catalysts as a function of size of ZnCr$_2$O$_4$ spinel oxides. As presented in Fig. 3a, the CO conversion and aromatics selectivity are greatly affected by the crystal size of ZnCr$_2$O$_4$. For example, the CO conversion reaches as high as 32.6% for ZnCr$_2$O$_4$ with a crystal size of 7.9 nm, but it dramatically declines to 3.4% when it grows to 32.1 nm. Correspondingly, the aromatics selectivity exhibits a similar trend, i.e., it is 76% over the former ZnCr$_2$O$_4$ but decreases to 50.4% over the latter. Meanwhile, the crystal size of ZnCr$_2$O$_4$ also significantly affects the STY of aromatics (Fig. 3b). It reaches as high as 4.40 mmol g$_{cat}^{-1}$ h^{-1} for 7.9 nm ZnCr$_2$O$_4$ crystals in contrast to only 0.31 mmol g$_{cat}^{-1}$ h^{-1} for those with a crystal size of 32.1 nm, enhancing by about 14.2 times. The same variation trend is also found for average particle size (Fig. S7).

Furthermore, we also noticed that the smaller the crystal size is, the higher oxygen vacancy concentration exists, which correlates monotonically with the CO conversion, aromatics selectivity and the STY of aromatics (Fig. 3). Oxygen vacancies are widely considered as active sites for CO hydrogenation activation in syngas conversion [1,16,22,28,29], which can influence the formation of surface intermediate species over oxides. This could be the intrinsic reason for the size effect of oxides on the catalytic performance for STA reaction.

Therefore, in order to obtain further insights into the size−performance relationship, the *in situ* diffuse reflectance infrared Fourier transform spectroscopy (DRIFTS) was employed to monitor the evolution of surface intermediate species over different ZnCr$_2$O$_4$ oxides. As illustrated in Fig. 4a−d, the adsorbed surface formate species (2957, 2870, 2743, 1578 and 1358 cm^{-1}) [21,37,38] and carbonate/bicarbonate species (1492, 1380 and 1305 cm^{-1}) [21,29,38] are clearly identified over all the ZnCr$_2$O$_4$ oxides after exposing to the syngas atmosphere under reaction condition, it has been widely reported that these active C$_1$ oxygenated species are regarded as the crucial intermediate species. These active oxygenated intermediates can be further transformed to form MeOH, DME and olefins intermediates [21,23,37], or/and carbonyl compounds intermediates [38,39], which can be consumed by H-ZSM-5 (Fig. S8) and continuously converted to generate aromatics in H-ZSM-5 finally [21,23,38,39]. Noticeably, when tracking the intensity variation of the IR
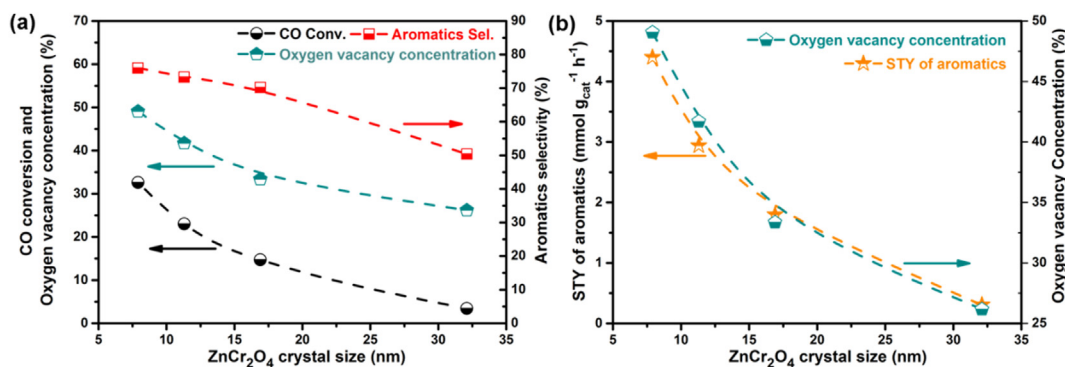

Fig. 3. Size−performance relationship. (a) The CO conversion, aromatics selectivity and the oxygen vacancy concentration as a function of the crystal size of ZnCr$_2$O$_4$ oxide. (b) The STY of aromatics and the oxygen vacancy concentration as a function of the crystal size of ZnCr$_2$O$_4$ oxide. The data correspond to Tables 1 and 2.
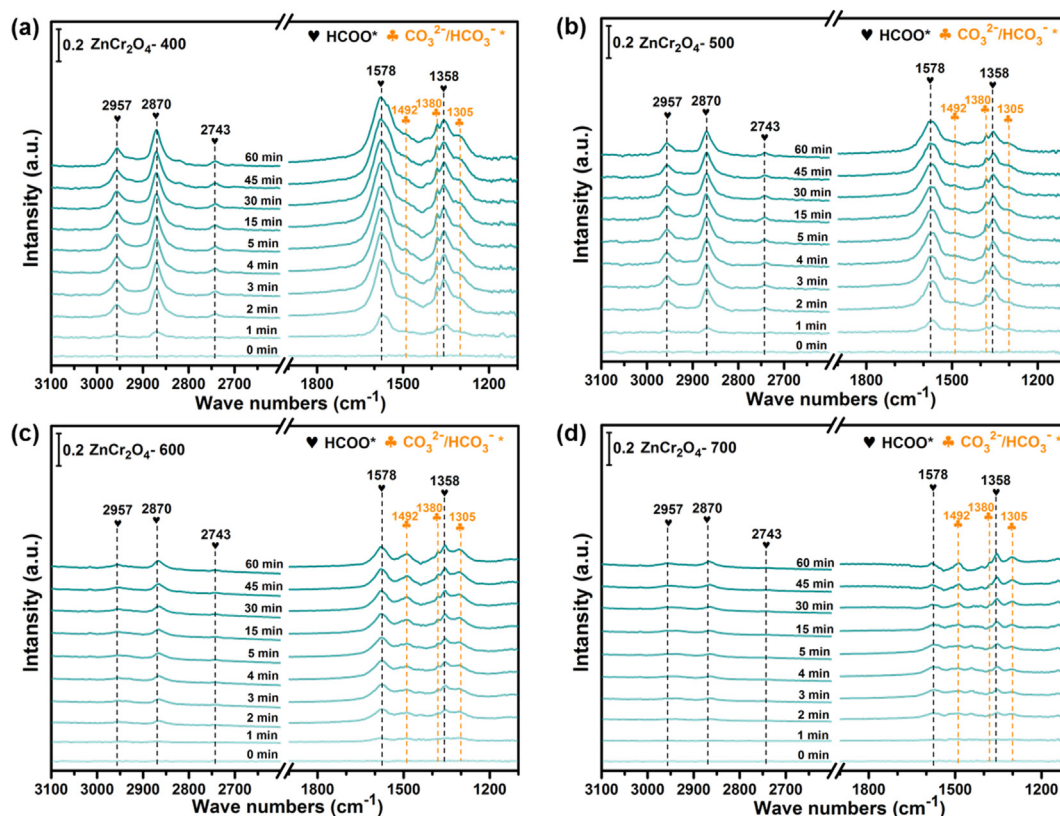
Fig. 4. *In situ* DRIFT observation for various oxides. (a) *In situ* DRIFT spectra for the CO hydrogenation over ZnCr$_2$O$_4$-400 oxide. (b) *In situ* DRIFT spectra for the CO hydrogenation over ZnCr$_2$O$_4$-500 oxide. (c) *In situ* DRIFT spectra for the CO hydrogenation over ZnCr$_2$O$_4$-600 oxide. (d) *In situ* DRIFT spectra for the CO hydrogenation over ZnCr$_2$O$_4$-700 oxide. The samples were exposed to the syngas of CO/H$_2$/Ar = 47.5/47.5/5 (5 mL min^{-1}) at 390 °C for 60 min.

signals for these surface intermediate species, it can be seen that the formation of these intermediate species over ZnCr$_2$O$_4$-400 is extremely faster and the corresponding intensity is also significantly stronger, followed by ZnCr$_2$O$_4$-500, ZnCr$_2$O$_4$-600, and ZnCr$_2$O$_4$-700 (Fig. 4a−d), which is well consistent with the above-mentioned catalytic performance (Table 2 and Fig. 3).

According to the results found above, we summarize the reasonable reason for the size effect of oxides on the catalytic performance for STA reaction: (1) The ZnCr$_2$O$_4$ oxides with smaller size and larger specific surface area can result in more surface defect sites (higher oxygen vacancy concentration), which are widely considered as active sites for CO hydrogenation activation in syngas conversion [1,16,22,28,29], thus resulting in higher CO conversion. (2) Syngas can be activated over oxygen vacancies of oxides to form C$_1$ oxygenated intermediate species [21,27,37,38], which can be further transformed by H-ZSM-5 to produce aromatics [21,23,38]. ZnCr$_2$O$_4$ oxides with smaller size and higher oxygen vacancy concentration can lead to the rapid formation of more C$_1$ oxygenated intermediate species, thus resulting in higher aromatics selectivity and higher STY of aromatics. The above results demonstrate that smaller ZnCr$_2$O$_4$ particles undoubtedly have a beneficial effect on the catalytic performance for STA reaction. Additionally, based on the understanding of the

size−performance relationship, ZnCr$_2$O$_4$-400 with a smaller size mixing with H-ZSM-5 can achieve as high as 4.79 mmol g$_{cat}^{-1}$ h^{-1} of aromatics STY, which outperforms the previously reported some typical catalysts (Fig. S1 and Table S1) [12–19,40–44].

4. Conclusion

In conclusion, we investigated the size effect of ZnCr$_2$O$_4$ spinel oxide in oxide-zeolite composite catalysts for syngas to aromatics (STA) reaction. The CO conversion, aromatics selectivity and space-time yield (STY) of aromatics are all significantly improved when the crystal size of ZnCr$_2$O$_4$ oxide decreases, which can mainly ascribe to the higher oxygen vacancy concentration and thus the rapid generation of more C$_1$ oxygenated intermediate species. Based on the understanding of the size−performance relationship, ZnCr$_2$O$_4$-400 with a smaller size mixing with H-ZSM-5 can achieve 32.6% CO conversion with 76% aromatics selectivity. The STY of aromatics reaches as high as 4.79 mmol g$_{cat}^{-1}$ h^{-1}, which exceeds the previously reported some typical catalysts. These results demonstrate the importance of the oxide size in oxide-zeolite composite catalysts for STA reaction and may be helpful to design more efficient catalysts for conversion of syngas to aromatics.

Declaration of competing interest

The authors declare that they have no known competing financial interests or personal relationships that could have appeared to influence the work reported in this paper.

Acknowledgments

Appendix A. Supplementary data

Supplementary data to this article can be found online at https://doi.org/10.1016/j.gee.2021.07.003.

References

[1] W. Zhou, K. Cheng, J. Kang, C. Zhou, V. Subramanian, Q. Zhang, Y. Wang, Chem. Soc. Rev. 48 (2019) 3193−3228.
[2] X.L. Yang, X. Su, D. Chen, T. Zhang, Y.Q. Huang, Chin. J. Catal. 41 (2020) 561−573.
[3] A.M. Niziolek, O. Onel, Y.A. Guzman, C.A. Floudas, Energy Fuels 30 (2016) 4970−4998.
[4] Y.M. Jia, J.W. Wang, K. Zhang, S.B. Liu, G.L. Chen, Y.F. Yang, C.M. Ding, P. Liu, Catal. Sci. Technol. 7 (2017) 1776−1791.
[5] S. Kasipandi, J.W. Bae, Adv. Mater. 31 (2019) 1803390.
[6] R.A. Friedel, R.B. Anderson, J. Am. Chem. Soc. 72 (1950) 1212−1215.
[7] M.E. Dry, J. Chem. Technol. Biotechnol. 77 (2002) 43−50.
[8] Q.G. Yan, Y.W. Lu, C.X. Wan, J. Han, J. Rodriguez, J.J. Yin, F. Yu, Energy Fuels 28 (2014) 2027−2034.
[9] N. Guan, Y. Liu, M. Zhang, Catal. Today 30 (1996) 207−213.
[10] B. Zhao, P. Zhai, P.F. Wang, J.Q. Li, T. Li, M. Peng, M. Zhao, G. Hu, Y. Yang, Y.W. Li, Q.W. Zhang, W.B. Fan, D. Ma, Inside Chem. 3 (2017) 323−333.
[11] Y. Xu, J. Liu, J. Wang, G. Ma, J. Lin, Y. Yang, Y. Li, C. Zhang, M. Ding, ACS Catal. 9 (2019) 5147−5156.
[12] K. Cheng, W. Zhou, J.C. Kang, S. He, S.L. Shi, Q.H. Zhang, Y. Pan, W. Wen, Y. Wang, Inside Chem. 3 (2017) 334−347.
[13] J.H. Yang, X.L. Pan, F. Jiao, J. Li, X.H. Bao, Chem. Commun. 53 (2017) 11146−11149.
[14] J.H. Yang, K. Gong, D.Y. Miao, F. Jiao, X.L. Pan, X.J. Meng, F.S. Xiao, X.H. Bao, J. Energy Chem. 35 (2019) 44−48.
[15] X.L. Yang, T. Sun, J.G. Ma, X. Su, R.F. Wang, Y.R. Zhang, H.M. Duan, Y.Q. Huang, T. Zhang, J. Energy Chem. 35 (2019) 60−65.
[16] Z. Huang, S. Wang, F. Qin, L. Huang, Y.H. Yue, W.M. Hua, M.H. Qiao, H.Y. He, W. Shen, H.L. Xu, ChemCatChem 10 (2018) 4519−4524.
[17] Y. Fu, Y.M. Ni, W.L. Zhu, Z.M. Liu, J. Catal. 383 (2020) 97−102.
[18] D.Y. Miao, Y. Ding, T. Yu, J. Li, X.L. Pan, X.H. Bao, ACS Catal. 10 (2020) 7389−7397.
[19] M.T. Arslan, B.A. Qureshi, S.Z.A. Gilani, D.L. Cai, Y.H. Ma, M. Usman, X. Chen, Y. Wang, F. Wei, ACS Catal. 9 (2019) 2203−2212.
[20] C. Liu, J.J. Su, S. Liu, H.B. Zhou, X.H. Yuan, Y.C. Ye, Y. Wang, W.Q. Jiao, L. Zhang, Y.Q. Lu, Y.D. Wang, H.Y. He, Z.K. Xie, ACS Catal. 10 (2020) 15227−15237.
[21] C. Zhou, J.Q. Shi, W. Zhou, K. Cheng, Q.H. Zhang, J.C. Kang, Y. Wang, ACS Catal. 10 (2020) 302−310.
[22] X.L. Liu, M.H. Wang, C. Zhou, W. Zhou, K. Cheng, J.C. Kang, Q.H. Zhang, W.P. Deng, Y. Wang, Chem. Commun. 54 (2018) 140−143.
[23] Y.M. Ni, Z.Y. Chen, Y. Fu, Y. Liu, W.L. Zhu, Z.M. Liu, Nat. Commun. 9 (2018) 3457.
[24] L.Y. Wang, X.F. Gao, Y.X. Bai, M.H. Tan, K. Sun, T. Zhang, Y.Q. Wu, J.X. Pan, H.J. Xie, Y.S. Tan, Fuel 253 (2019) 1570−1577.
[25] D. Xu, X.L. Hong, G.L. Liu, J. Catal. 393 (2021) 207−214.
[26] S.K. Pardeshi, A.B. Patil, J. Mol. Catal. Chem. 308 (2009) 32−40.
[27] W. Ao, J. Li, H. Yang, X. Zeng, X. Ma, Powder Technol. 168 (2006) 148−151.
[28] F. Jiao, J.J. Li, X.L. Pan, J.P. Xiao, H.B. Li, H. Ma, M.M. Wei, Y. Pan, Z.Y. Zhou, M.R. Li, S. Miao, J. Li, Y.F. Zhu, D. Xiao, T. He, J.H. Yang, F. Qi, Q. Fu, X.H. Bao, Science 351 (2016) 1065−1068.
[29] Y.F. Zhu, X.L. Pan, F. Jiao, J. Li, J.H. Yang, M.Z. Ding, Y. Han, Z. Liu, X.H. Bao, ACS Catal. 7 (2017) 2800−2804.
[30] C. Yang, J. Wang, H.L. Fan, S.G. Ju, J. Mi, C. Huo, Fuel 215 (2018) 695−703.
[31] F.C. Lei, Y.F. Sun, K.T. Liu, S. Gao, L. Liang, B.C. Pan, Y. Xie, J. Am. Chem. Soc. 136 (2014) 6826−6829.
[32] Z.L. Wang, X. Mao, P. Chen, M. Xiao, S.A. Monny, S.C. Wang, M. Konarova, A.J. Du, L.Z. Wang, Angew. Chem. Int. Ed. 58 (2019) 1030−1034.
[33] E. Kadossov, U. Burghaus, J. Phys. Chem. C 112 (2008) 7390−7400.
[34] S. Azad, M.H. Engelhard, L.Q. Wang, J. Phys. Chem. B 109 (2005) 10327−10331.
[35] W.H. Li, X.W. Nie, X. Jiang, A.F. Zhang, F.S. Ding, M. Liu, Z.M. Liu, X.W. Guo, C.S. Song, Appl. Catal. B Environ. 220 (2018) 397−408.
[36] J. Liu, Y. Liu, Y.M. Ni, H.C. Liu, W.L. Zhu, Z.M. Liu, Catal. Sci. Technol. 10 (2020) 1739−1746.
[37] X.L. Liu, W. Zhou, Y.D. Yang, K. Cheng, J.C. Kang, L. Zhang, G.Q. Zhang, X.J. Min, Q.H. Zhang, Y. Wang, Chem. Sci. 9 (2018) 4708−4718.
[38] M.T. Arslan, B. Ali, S.Z.A. Gilani, Y.L. Hou, Q. Wang, D.L. Cai, Y. Wang, F. Wei, ACS Catal. 10 (2020) 2477−2488.
[39] Z.Y. Chen, Y.M. Ni, F.L. Wen, Z.Q. Zhou, W.L. Zhu, Z.M. Liu, Chin. J. Catal. 42 (2021) 835−843.
[40] S. Wang, Z. Huang, Y.J. Luo, J.H. Wang, Y. Fang, W.M. Hua, Y.H. Yue, H.L. Xu, W. Shen, Catal. Sci. Technol. 10 (2020) 6562−6572.
[41] J.G. Liu, Y.R. He, L.L. Yan, K. Li, C.H. Zhang, H.W. Xiang, X.D. Wen, Y.W. Li, Catal. Sci. Technol. 9 (2019) 2982−2992.
[42] S.Z.A. Gilani, L. Lu, M.T. Arslan, B. Ali, Q. Wang, F. Wei, Catal. Sci. Technol. 10 (2020) 3366−3375.
[43] C. Liu, S. Liu, H.B. Zhou, J.J. Su, W.Q. Jiao, L. Zhang, Y.D. Wang, H.Y. He, Z.K. Xie, Appl. Catal. Gen. 585 (2019) 117206.
[44] Y. Wang, W.Z. Gao, K.Z. Wang, X.H. Gao, B.Z. Zhang, H. Zhao, Q.X. Ma, P.P. Zhang, G.H. Yang, M.B. Wu, N. Tsubaki, Chem. Sci. DOI: 10.1039/d1sc01859k.